RSC Advances

PAPER

View Article Online
View Journal | View Issue

Cite this: *RSC Adv.*, 2023, **13**, 24064

A novel cationic covalent organic framework as adsorbent for simultaneous removal of methyl orange and hexavalent chromium†

Chang Du,‡ Xiaodi Chen,‡ Hongping Wu, Zilu Pan, Chunyan Chen,* Guanqun Zhong* and Changqun Cai

Received 3rd June 2023
Accepted 23rd July 2023

DOI: 10.1039/d3ra03726f

rsc.li/rsc-advances

The simultaneous removal of toxic, carcinogenic organic dyes and metal ions from water by one material offers significant advantages when fast, facile, and robust water purification is required. Ionic covalent organic frameworks (ICOFs) have the combined properties of COFs and ion exchange resins and are expected to achieve simultaneous capture of heavy metal ions and organic dyes from water. Herein, a novel guanidinium-based ICOF was synthesized using a solvothermal method. Benefitting from the cationic character, porosity and nanoscale pore size of ICOFs, the adsorbent exhibited high simultaneous adsorption capacities of 290 mg g^{-1} and 158 mg g^{-1} for methyl orange (MO) and Cr(VI), respectively, and retained more than 90% adsorption capacity after six adsorption–desorption cycles. In addition, based on dual control of size-exclusion and charge-selection, precisely selective adsorption is achieved towards diverse mixed anionic and cationic pollutants. This strategy offers a practical solution for COFs to confront environmental pollution issues.

1 Introduction

With the increasing industrialization of the global economy, organic dyes are frequently being used for coloring in various industries, such as textiles, dyeing, leather, and papermaking, resulting in a huge amount of dye-containing wastewater.[1] This kind of effluent commonly contains potentially toxic metal ions as well.[2] Thus, these effluents pose serious threats to public health and the environment, due to their complex components, high colourity, potential mutagenicity, and poor biochemical purification ability.[3] As a widely used azo dye, methyl orange (MO) can lead to severe health problems like tachycardia, vomiting, cyanosis, jaundice, quadriplegia, and tissue necrosis.[4] On the other hand, Cr(VI) ions can cause diarrhea, vomiting, pulmonary congestions liver and kidney damage.[5] Presently, MO and Cr(VI) usually co-exist in some wastewater.[6] Therefore, the simultaneous removal of MO and Cr(VI) from industry effluent is urgently needed.

Various techniques have been applied for the individual removal of MO and Cr(VI).[6,7] Compared to electrolytic chemical treatment,[8] membrane separation,[9] chemical reduction,[10] and biological treatment,[11] adsorption is still a preferable approach due to its simplicity, low-cost, and effectiveness.[12] However, the commonly used adsorbents are mainly single MO adsorbents or Cr(VI) adsorbents. Due to their significantly different physicochemical properties,[13,14] few studies have focused on the simultaneous removal of MO and Cr(VI), and those adsorbents suffer from low capacity or low efficiency.[13] Therefore, the design and fabrication of efficient, stable, environment-friendly, and low-cost adsorbents for the simultaneous removal of MO and Cr(VI) is imperative.

Covalent organic frameworks (COFs) are crystalline porous materials formed by covalent bonding of organic monomers.[15] Benefiting from advantages of porosity, high surface area, adjustable pore size and easy functionalization of the pore surface, COFs have shown excellent performance in removing heavy metal ions[16–20] and organic dyes,[21–24] but the simultaneous removal of the toxic pollutants coexisting in printing and dyeing wastewater has been little investigated.[25] Ionic covalent organic frameworks (ICOFs) are an emerging class of functional materials that have the combined properties of COFs and porous ionic polymers (PiPs), and thus have the potential to effectively remove a variety of different contaminants, such as metal ions.[26]

Herein, a novel ICOF based on a positively charged triaminoguanidine chloride was produced to eliminate both MO and Cr(VI) from water simultaneously. The ICOF was characterized systematically. The adsorption equilibrium and binding kinetics of ICOF for MO and Cr(VI) in their single pollutant systems were studied, and its simultaneous adsorption capacity for MO and Cr(VI), as well as its reusability in binary systems,

Key Laboratory for Green Organic Synthesis and Application of Hunan Province, Key Laboratory of Environmentally Friendly Chemistry and Application of Ministry of Education, College of Chemistry, Xiangtan University, Xiangtan 411105, China. E-mail: chenchunyan@xtu.edu.cn; 15616727476@163.com

† Electronic supplementary information (ESI) available. See DOI: https://doi.org/10.1039/d3ra03726f

‡ Chang Du and Xiaodi Chen should be considered as first authors.

were examined. Moreover, the selective adsorption capacity of ICOF was discussed in detail. The results demonstrated excellent prospects for the development of ICOF as efficient and recyclable adsorbents for the simultaneous efficient removal of heavy metal ions and organic dyes in water treatment.

2 Experimental section

2.1. Synthesis of ICOF

ICOF was synthesized *via* Schiff base reaction between 5,5′-(1,4-phenylene) dipicolinaldehyde (12.97 mg, 0.045 mmol) and triaminoguanidinium chloride (TGCl, 4.22 mg, 0.03 mmol) in 1.1 mL of tetrahydrofuran (THF)/3 M HAc (1 : 0.1, v/v). The mixture was placed into a Pyrex tube (10 × 8 mm^2 and length 20 cm) and sonicated for 15 min. The mixture was degassed three times by freeze–pump–thaw cycles under liquid N_2, then the tube was sealed and heated at 120 °C for 3 days. ICOF was obtained as red precipitates. The product was collected by centrifugation and washed with DMF, water and THF and dried at 60 °C under vacuum overnight in *ca.* 86% isolated yield.

2.2. Adsorption experiments

2.2.1 Adsorption of MO and Cr(VI) in single pollutant systems. The adsorption performances of ICOF were evaluated by MO and Cr(VI), respectively. The adsorption experiments were performed using 3 mg of ICOF in 6 mL of MO dye or Cr(VI) ions solution, and then the solution was shaken for 24 h. The pH values were adjusted by using 0.1 M HCl or NaOH. After adsorption, the final concentrations of MO were measured using a UV-vis spectrophotometer at 462 nm and the residual Cr(VI) ions were measured using the 1,5-diphenylcarbazide method.[27] The adsorption capacities and removal efficiencies were calculated by using mass balance equations [eqn (1) and (2)]:

$$Q_e = \frac{c_0 - c_e}{m} \times V \quad (1)$$

$$\text{Removal}(\%) = \frac{c_0 - c_e}{c_0} \times 100\% \quad (2)$$

Q_e is the equilibrium adsorption capacity (mg g^{-1}), C_0 and C_e are the initial and equilibrium adsorbate concentrations, respectively (mg L^{-1}), V is the volume of the adsorbate solution (mL), and m is the mass of the ICOF (mg).

2.2.2 Simultaneous adsorption of MO and Cr(VI) in binary pollutant systems. The simultaneous removal experiments of MO and Cr(VI) were carried out at 310 K and the pH value of the binary adsorption experiments was set at 3. Other experimental conditions were similar to those in their single pollutant system as mentioned above, except for the coexistence of MO and Cr(VI) in solution.

2.2.3 Adsorbent recycling. The reusability of sorbent (ICOF) was estimated after the adsorption of MO and Cr(VI). After loading ICOF (3 mg) in a mixed solution of MO and Cr(VI) (pH = 3, 200 mg L^{-1}, 6 mL), the solid was separated by filtration and then eluted three times with ultrapure water. Subsequently, 30 mL of 0.5 M NaOH solution was added to the residual solid and stirred magnetically for 3 h. Afterward, the obtained solid was eluted three times with ultrapure water, and then 30 mL of 1.0 M HCl solution was added and stirred magnetically for 3 h. Finally, the adsorbent was collected by filtration and dried under vacuum at 60 °C for 2 h for the next round of adsorption.

3 Results and discussion

3.1. Characterization of the adsorbents

In this study, an ICOF with a positively charged backbone was produced by introducing a cationic guanidine groups into the framework. This positively charged backbone can strongly interact electrostatically with oppositely charged ionic contaminants, thus enhancing the adsorption capacity of the ICOF. The one-step synthesis scheme of the ICOF is described in Fig. 1.

The newly developed ICOF were further characterized using various spectroscopy and microscopy techniques. The occurrence of Schiff base reaction during the construction of ICOF was confirmed by the Fourier transform infrared spectrum (FT-IR) (Fig. 2a). The carbonyl stretching vibration peak (C=O, 1719 cm^{-1}) of the aldehyde monomer and the N–H stretching vibration peak (3329 cm^{-1}, 3201 cm^{-1}) of primary amines in the TGCl monomer disappeared in the corresponding product. Moreover, an obvious signal of C=N stretching bond (1623 cm^{-1}) appeared in ICOF after the condensation reaction, which reveals the successful formation of new imide bonds between aldehyde and amino groups in networks.

The crystalline structure of ICOF was analyzed according to the powder X-ray diffraction (PXRD) pattern. As shown in Fig. S1,† there was one broad characteristic peak at 2θ = 20–27°, which suggested its crystallinity was low. Concretely, the broad peak at 20–27° revealed that the π–π stacking between layers of the crystalline structure was poor, which was affected by the charge repulsion between guanidine groups and Cl^-.[26]

To investigate the morphology of ICOF at the nanoscale, it was characterized by scanning electron microscopy (SEM). It can be seen in Fig. 2b that the COF was an aggregate of many short nanofibers with a coral-like structure.

The porosity of the ICOF was further assessed in detail through N_2 adsorption–desorption experiments at 77 K (Fig. 2c). The Brunauer–Emmett–Teller (BET) surface area was calculated

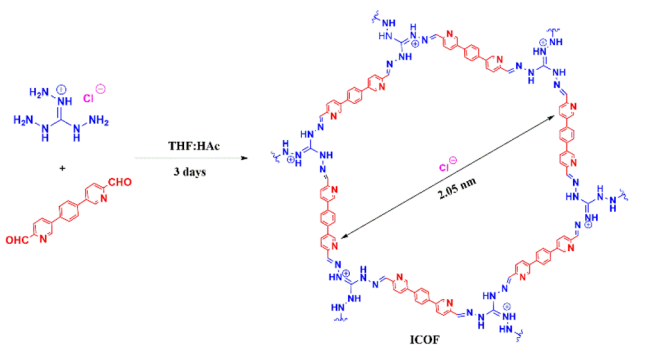

Fig. 1 Synthesis of ICOF.

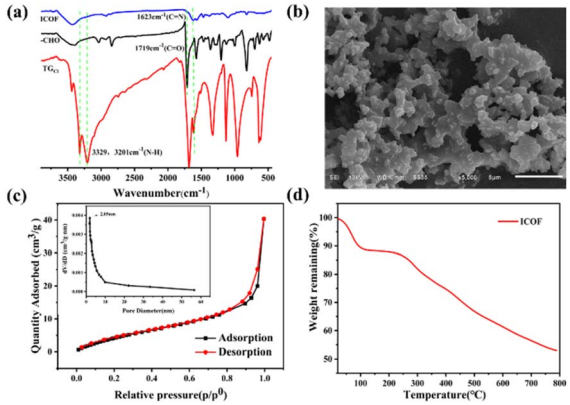

Fig. 2 (a) FTIR spectrum of ICOF, reactants –CHO and TGCl. (b) SEM images for ICOF. (c) N_2 adsorption isotherm (77 K) and pore size distribution profiles. (d) TGA curves of ICOF.

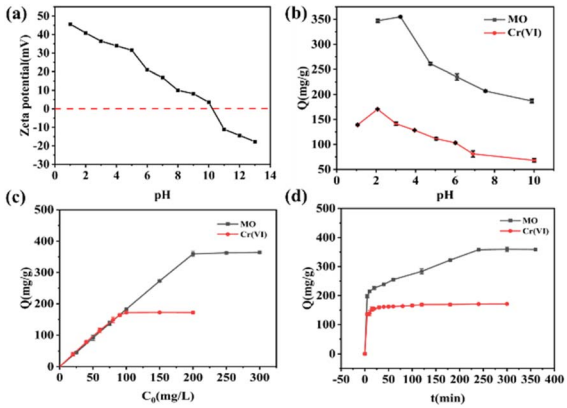

Fig. 3 (a) Zeta potential of ICOF under different pH conditions; (b) pH effects on MO and Cr(VI) uptake onto ICOF; (c) adsorption equilibrium of MO and Cr(VI) onto ICOF (initial concentration: 25–300 mg L^{-1} for MO and 25–100 mg L^{-1} for Cr(VI); adsorbent dose: 3 mg; volume: 6 mL; pH: 3 for MO and 2 for Cr(VI); temperature: 310 K); (d)adsorption kinetics of MO and Cr(VI) onto ICOF (initial concentration: 200 mg L^{-1} for MO and 100 mg L^{-1} for Cr(VI); adsorbent mass: 3 mg; volume: 6 mL; pH: 3 for MO and 2 for Cr(VI); temperature: 310 K).

to be 21.59 m^2 g^{-1}. The poor directional control of the guanidine units in the layers was likely responsible for the relatively low BET surface area of the ICOF, which was also observed in other ICOF.[28] The sorption isotherm belongs to type IV, which is indicative of mesoporous materials. The pore size distribution profile obtained from adsorption branch (Fig. 2c, inset) based on NLDFT method also indicates the dominant existence of mesopores in the ICOF structure, with the pore diameter of the ICOF centered at 2.05 nm.

The thermal gravimetric analysis (TGA) (Fig. 2d) was utilized to estimate the thermal stability of the ICOF, which is thermally stable below 278 °C with a minor loss of weight. The first weight loss (below 100 °C) corresponds to the elimination of absorbed water (about 10%).

3.2. Removal of MO and Cr(VI) in single pollutant system

3.2.1 pH effect. It is well known that the initial pH value of the aqueous solution can not only change the surface charges and ionization degrees of the ionic adsorption material, but also affect the species distribution of dyes and metal ions in the solution.[29] The zeta potentials of ICOF under different pH conditions were measured and its pHzpc (point of zero charge) was about 10 (Fig. 3a). The surface charge of the ICOF was positive at pH < pHzpc, while it was negative at pH > pHzpc. The wider positive range would be beneficial for the adsorption of anionic contaminants.

The effects of solution pH on the adsorption performance of MO and Cr(VI) on the ICOF were shown in Fig. 3b. It's clearly observed that the adsorption capacity of both MO and Cr(VI) was highly pH dependent. The adsorption capacity of both MO and Cr(VI) increased and then decreased with an increase in pH. The maximum adsorption capacity of MO was attained at pH = 3.23, while that of Cr(VI) was reached at pH = 2. For the adsorbent, the number of surface charges in ICOF decreases with an increasing solution pH due to a partial deprotonation of the guanidinium ions present in the framework, leading to a weakened electrostatic interaction and diminished adsorption capacity of negatively charged substances. For MO, it is exists mainly as an azo structure at pH > pK_a (3.57) and as a hydrazone structure at pH < pK_a (Fig. S2†). The adsorption capacity of MO decreased when the pH was below 3.23, which could be attributed to the steric effect of dimethyl amino groups and the electrostatic repulsion between protonated dimethyl amino groups and the adsorbent. In addition, MO was found to form a dimer under acidic conditions, and this dimer showed electroneutrality, which reduced the interaction with ICOF.Consequently, the optimal pH value for removal of MO by ICOF was chosen as 3.0. For Cr(VI), it exists in water in the form of CrO_4^{2-}, $HCrO_4^-$, $Cr_2O_7^{2-}$ and H_2CrO_4, depending on solution pH. When the pH is lower than 2.0, the neutral H_2CrO_4 in water increases, weakening the electrostatic interactions with the adsorbents and thus decreasing its adsorption capacity.[30] Therefore, the optimal pH value appears at 2.0 which was also selected for the subsequent experiments.

3.2.2 Adsorption equilibrium. Adsorption isotherms of MO and Cr(VI) on ICOF were measured and shown in Fig. 3c. It is obvious that the adsorption amount of MO and Cr(VI) increase with the increase of their initial concentrations. For MO, at a concentration of 100 mg L^{-1}, the removal rate reaches 99.76%. The adsorption gradually approaches saturation when the initial concentration exceeds 200 mg L^{-1} and the maximum adsorption capacity can reach up to 375 mg g^{-1}. As for Cr(VI), its saturated adsorption concentration is at 100 mg L^{-1} with a maximum adsorption capacity of 172 mg g^{-1}. To further understand the adsorption process and adsorption mechanism, Langmuir and Freundlich models[31] were employed to fit the experimental data (Fig. S3†). Their equations are expressed in the below (3) and (4).

$$\frac{c_e}{Q_e} = \frac{K_s}{Q_m} + \frac{c_e}{Q_m K_s} \quad (3)$$

$$\log Q_e = \log K_f + \frac{1}{n}\log c_e \quad (4)$$

Where Q_m (mg g^{-1}) and Q_e (mg g^{-1}) represent the maximum adsorption capacity and equilibrium adsorption capacity, respectively. C_e (mg L^{-1}) is the equilibrium concentration. K_s (mg L^{-1}) is the Langmuir constant, and K_f (g mg^{-1}) and n are the Freundlich constants concerned with the adsorption capacity and adsorption intensity, respectively.

The final fitted results are listed in Table S1.† It can be seen that the linear correlation coefficients (R^2) of Langmuir model is much higher than that of Freundlich. Furthermore, the Q_m of adsorbates on ICOF calculated by Langmuir model are all much closer to the experimental results. Therefore, the Langmuir model can better describe their adsorption behaviors, and the adsorption of MO and Cr on ICOF is monolayer adsorption.

3.2.3 Adsorption kinetics. The adsorption kinetics of ICOF for MO and Cr(VI) were studied at 310 K, respectively. The results are all shown in Fig. 3d MO adsorption on ICOF was fairly rapid within the first 5 min and achieved equilibrium after 2.5 h. Meanwhile, the adsorption of Cr(VI) on ICOF quickly reached equilibrium after 50 min. The new adsorbent presented a fast adsorption kinetics for MO and Cr(VI) with an equilibrium time of less than 3 h.

To further investigate the adsorption mechanism, simulation for these kinetic data was conducted on the basis of pseudo-first-order and pseudo-second-order models,[32] respectively (Fig. S4†). The models were expressed respectively by eqn (5) and (6) listed as follows.

$$\ln(Q_e - Q_t) = \ln Q_e - k_1 t \quad (5)$$

$$\frac{t}{Q_t} = \frac{1}{k_2 Q_e^2} + \frac{t}{Q_e} \quad (6)$$

Where Q_e and Q_t (mg g^{-1}) are the amounts of pollutants adsorbed onto the adsorbent at equilibrium and at time t (min), respectively, k_1 (min^{-1}) and k_2 (g mg^{-1} min^{-1}) are the rate constants of the pseudo-first order and pseudo-second order models, respectively.

The fitted parameters are all listed in Table S2.† Considering the correlation coefficients (R^2), the pseudo-second-order model can better fit the adsorption kinetics of MO and Cr(VI) by ICOF. It indicates that chemisorption is the rate controlling mechanism in the adsorption of these two pollutants, which is fully consistent with those drawn from adsorption isotherms analysis as mentioned above.

3.2.4 Effects of coexisting ions. Due to the formation of strong ion pairs between guanidinium and oxoanions through directional, noncovalent hydrogen bonding interactions and electrostatic forces, different types of anions may compete with Cr(VI) or MO, thus affecting the performance of absorbents. To understand the principles of competition, ubiquitous chloride ions (NaCl), trihedral nitrate ions ($NaNO_3$), negative divalent tetrahedral sulfate ions (Na_2SO_4) and negative bicarbonate ions ($NaHCO_3$) were selected for coexistence ions experiments. Meanwhile, as ionic strength may affect the adsorption, three different concentration gradients were selected.

According to Fig. 4a, in the presence of competing anions, *i.e.*, NO_3^-, Cl^- and SO_4^{2-} ions, no significant inhibition of the adsorption capacities of the ICOF for MO was observed. However, due to the alkaline nature of the aqueous solution of HCO_3^-, the electrostatic interaction between the adsorbate and the adsorbent is weakened, significantly decreasing the adsorption capacity of ICOF. As is shown in Fig. 4b, Cl^- and NO_3^- had little impact on Cr(VI) adsorption owing to the non-tetrahedral structure, while SO_4^{2-}, with the tetrahedral structure decreased the adsorption performance of ICOF at higher concentrations. Seipp's[33] work indicated that the binding affinity of guanidinium receptors for anions depends on hydrogen bond donating capacities and coulombic stabilization. Thus, it could be explained that SO_4^{2-} with stronger electronegativity exhibited a higher binding affinity for guanidinium groups, because it has higher electronic charge. As for HCO_3^-, the reason affecting the amount of Cr(VI) adsorbed on ICOF is the same as for MO.

3.3. Removal of MO and Cr(VI) in binary pollutant system

3.3.1 pH effects. The competitive adsorption experiments were carried out in MO and Cr(VI) aqueous mixtures at a concentration of 200 mg L^{-1} under different pH levels. The final results are presented in Fig. 5a, showing the good simultaneous binding ability of ICOF for MO and Cr(VI). Although the adsorption capacities were slightly decreased in both simultaneous adsorption experiments.*i.e.*, about 23% for Cr(VI) and nearly 44% for MO, these results are still acceptable. The pH dependence of MO and Cr(VI) uptakes are similar to those in their respective single pollutant systems as shown in Fig. 3b. The optimal pH value appears at 3.0, which was also selected for the subsequent experiments.

3.3.2 Adsorption isotherms. To further investigate the competitive adsorption process, the adsorption isotherms of MO and Cr(VI) on ICOF in binary systems were measured at pH 3.0 and 298 K, 308 K, and 318 K, respectively, and shown in Fig. 5c and d. Evidently, the absorption capacity of MO and Cr(VI) decreased significantly compared to single pollutant system. And as the temperature increases, the adsorption capacity of MO and Cr(VI) increases substantially. Interestingly, the MO and Cr(VI) maximum adsorption capacity in the binary

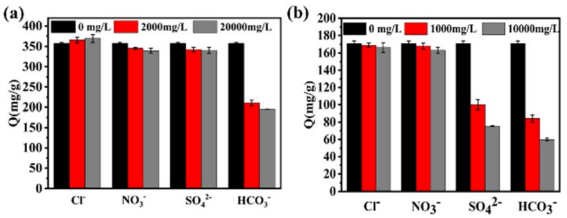

Fig. 4 Influence of co-ions on the elimination of MO and Cr(VI) on ICOF. (a) MO (C_{MO} = 200 mg L^{-1} and CM = 0, 2000, or 20 000 mg L^{-1} each; adsorbent dose: 3 mg; volume: 6 mL; pH: 3; temperature: 310 K). (b) Cr(VI) ($C_{Cr(VI)}$ = 100 mg L^{-1} and CM = 0, 1000, or 10 000 mg L^{-1} each; adsorbent dose: 3 mg; volume: 6 mL; pH: 2; temperature: 310 K).

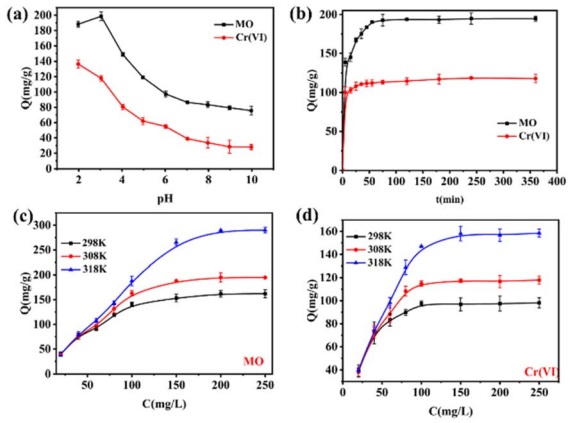

Fig. 5 (a)Effects of pH on MO and Cr(VI) onto ICOF. (initial concentration: 200 mg L^{-1}; adsorbent mass: 3 mg; volume: 6 mL; pH: 2–10; temperature: 310 K); (b) adsorption kinetics of MO and Cr(VI) onto ICOF (initial concentration: 200 mg L^{-1}; adsorbent dose: 3 mg; volume: 6 mL; pH: 3; temperature: 310 K). (c)Adsorption isotherms of MO and (d) Cr(VI) onto ICOF (initial concentration: 20–250 mg L^{-1}; adsorbent mass: 3 mg; volume: 6 mL; pH: 3; temperature: 298 K, 308 K, and 318 K).

pollutant system was found to be 290 and 158 mg g^{-1} at 318 K, respectively, which is higher than previous reported studies (Table S3†).

According to the regression coefficient (R^2), the Langmuir model is more consistent with the adsorption behavior of MO and Cr(VI) on the ICOF than the Freundlich model (Table S4 and Fig. S5†), indicating the homogeneous adsorption sites and monolayer interaction between the ICOF and adsorbates (MO and Cr(VI)), and this is consistent with the single pollutant system. These results clearly show that the ICOF can be used to simultaneously remove MO and Cr(VI) from the mixed solution.

Thermodynamic studies can offer meritorious data, including a calculation of the thermodynamic parameters ΔG^0 (kJ mol^{-1}), ΔH^0 (kJ mol^{-1}) and ΔS^0(kJ mol^{-1} K^{-1}).[34] These parameters were calculated by the following equations:

$$K_c = \frac{Q_e}{C_e} \quad (7)$$

$$\Delta G^0 = -RT \ln K_c \quad (8)$$

$$\ln K_c = -\frac{\Delta H^0}{RT} + \frac{\Delta S^0}{R} \quad (9)$$

Where T (K) is the absolute temperature, R (8.314 J × mol^{-1} × K^{-1}) is the universal gas constant, K_c is the adsorption equilibrium constant (L g^{-1}), and C_e is the equilibrium concentration of the pollutants in solution (mg g^{-1}). ΔG^0, ΔH^0, and ΔS^0 are the standard Gibb's free energy, enthalpy changes, and entropy, respectively. It can be seen that the K_c values increased with higher temperatures from 298 K to 318 K (Table S5†), indicating the endothermic nature of the adsorption ($\Delta H^0 > 0$). The negative value of ΔG^0 also verifies that the adsorption process is spontaneous. The absolute value of ΔG^0 rises with increasing temperature, demonstrating that higher temperatures promote the spontaneity of the adsorption reaction.

3.3.3 Adsorption kinetics. In the binary pollutant system, the adsorption efficiencies of MO and Cr(VI) were faster than those in the single pollutant system, reaching equilibrium in 75 min for MO and 35 min for Cr(VI), respectively (Fig. 5b).Similar to the single pollutant system, it conforms to the pseudo-second-order kinetic model (Fig. S6 and Table S6†), indicating a chemical adsorption process.

3.4. Adsorption selectivity

3.4.1 Adsorption selectivity of ICOF for different dyes and metal ions. Six dyes with different properties were used to evaluate the adsorption selectivity of ICOF for dyes, including the anionic dyes: methyl orange (MO) and potassium permanganate (PP); the neutral dyes: nile red (NR) and *p*-nitroaniline (NA) and the cationic dyes: rhodamine B (RhB) and methylene blue (MB). Their corresponding chemical structures and properties are shown in Fig. S7 and Table S7.† The adsorption capacities of the ICOF toward six dyes were shown in Fig. S8(a–f).† For anionic dyes, the characteristic absorption bands of MO and PP were completely disappeared after adsorption, while for neutral and cationic dyes, only the intensity of the characteristic absorption spectrum of NR was diminished, the intensities of NR, RhB, and MB remained nearly the same. The color changes of different dye solutions before and after adsorption were also observed clearly *via* naked eyes from the inset photographs of Fig. 8. The removal rates of different dyes were determined and shown in Fig. S9.† The result shows that the ICOF can remove anionic dyes MO and PP up to 99.7% and 99.8%, respectively, which is mainly attributed to its cationic nature and suitable pore size. The removal rates of neutral dyes NR and NA are 2.61% and 29.3%, respectively. The absorption efficiency of neutral dyes is mainly attributed to the molecular size sieving effect, and the removal rates were in good agreement with their molecular sizes. Whereas for cationic dyes RB and MB, the removal rates are 1.88% and 3.94%, respectively. Due to the strong electrostatic repulsion interaction between positively charged ICOF and cationic dye, dye molecules will be unable to enter the pore channels of ICOF. Furthermore, the selective adsorption of ICOF on MO from a mixed solution of MO and MB, as shown in Fig. 6, further demonstrated the selectivity of the positively

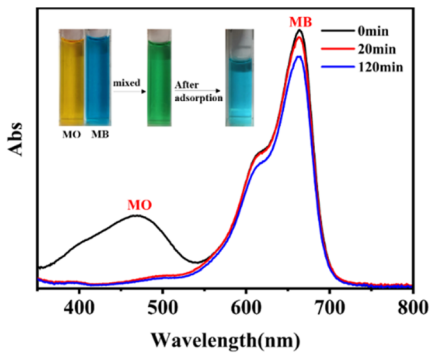

Fig. 6 Dye selectivity of ICOF with mixed dye (MB and MO) initial concentration: 20 mg L^{-1}; adsorbent mass: 2 mg; volume: 6 mL.

charged ICOF on negatively charged adsorbates. The above experimental results show that ICOF has an impressive capacity to selective adsorption of different dye molecules and metal ions, a process that is regulated by both electrostatic interaction and the restriction of the pore size.

The adsorption ability of the ICOF toward different target metal ions was also evaluated. As shown in Fig. S8(g) and (h),† the characteristics absorption band of Cr(VI) was completely disappeared after absorption by ICOF. But for Cu^{2+}, it presented a smaller decline in the intensity of characteristics absorption spectra. Meanwhile, the removal rate of $Cr_2O_7^{2-}$ was 98.85%, much higher than that of Cu^{2+} (11.88%), which is fully demonstrates the charge discrimination ability of the ICOF (Fig. S10†).

3.4.2 Adsorption selectivity of different adsorbents with different pore sizes and charges for MO and Cr(VI). To further verify the high adsorption selectivity of this new adsorbent, several adsorbents with similar structures but different pore sizes and charges (Fig. S11†) were synthesized and a competitive test was conducted on the mixed solution of MO and Cr(VI) (Fig. 7). TpPa COF is a neutral COF material, possessed a low uptake capacity for MO and Cr(VI) from water. Compared with TpPa COF, TpTGCl COF, BpyTGCl COF and ICOF are ionic COF materials, and the adsorption capacity of MO and Cr(VI) is significantly increased, which proves the important role of electrostatic interaction in the adsorption process. The difference between TpTGCl COF, BpyTGCl COF and ICOF is that their aldehyde monomers have different lengths, resulting in different pore sizes of the COF materials. This affects the adsorption efficiency as larger dye molecules may be hindered from entering the smaller pore size materials. The above analysis proves that the ICOF has a unique adsorption mode that relies on dual control of physical size and electrostatic charge. The competitive test results also further demonstrate that the new adsorbent has a good binding selectivity for anionic dye and oxyanions.

3.5. Recyclability

Reusability of adsorbent is the main factor determining its economic feasibility for application in real water treatment. In order to evaluate the recovery performance of ICOF after adsorption of MO and Cr(VI), 0.5 M NaOH solution and 1.0 M HCl solution were used to regenerate it successively. As shown in Fig. S12,† the regenerated ICOF retained a 90% removal capacity for MO and Cr(VI) in the binary pollutant system after five consecutive cycles. This confirmed that the ICOF was a reliable and reusable adsorbent.

3.6. Adsorption mechanism

In order to further investigate the adsorption mechanism of MO and Cr on the ICOF, XPS analysis of ICOF before and after adsorption was provided in the revised manuscript. As shown in Fig. 8, ICOF mainly contains three elements: C, N, and O, where element O exists in the defective part of ICOF. In the full-range XPS map of ICOF after adsorption, the binding energies of the main elements were almost unchanged (Table S8†). The peak corresponding to the element S was observed at 163.4 eV, and the peak corresponding to element Cr was observed at 577 eV, indicating that MO and Cr were successfully adsorbed on the surface of ICOF.

Furthermore, the Cr $2p_{3/2}$ and Cr $2p_{1/2}$ XPS data for ICOF after adsorption of Cr(VI) are given in Fig. S13.† The high binding energy features (~586.77 eV) and low binding energy features (~577.27 eV) correspond to Cr(III) $2p_{1/2}$ and Cr(III) $2p_{3/2}$ orbitals, respectively. The appearance of the characteristic Cr(III) peak may be attributed to the water-insoluble Cr(III) compounds which may be generated due to the alteration of the local ambient reduction potential of the ICOF during the drying process of the samples required for the XPS measurements. In addition, as the zeta potential of ICOF becomes negative, its adsorption of MO and Cr (VI) decreases, and it can be inferred that the adsorption of MO and Cr(VI) on the ICOF mainly relies on electrostatic interactions.

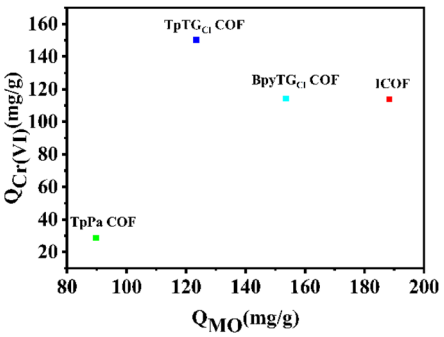

Fig. 7 The adsorption capacity of different adsorbents for MO and Cr(VI) in the binary mixed pollutant system (initial concentration: 200 mg L^{-1}; adsorbent dose: 3 mg; volume: 6 mL; pH: 3; temperature: 310 K).

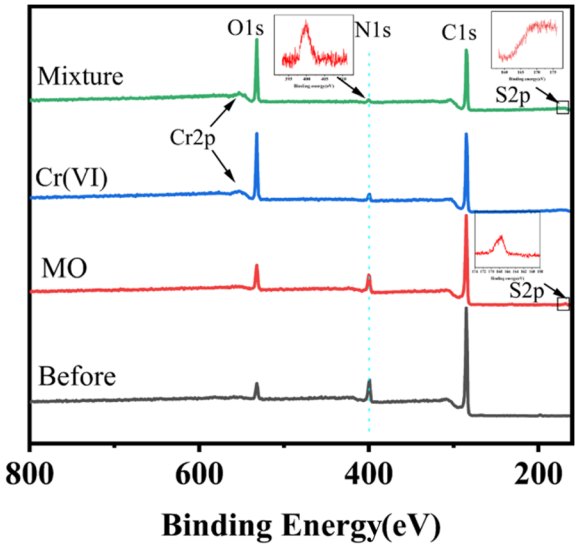

Fig. 8 XPS spectra of ICOF before and after adsorption of Cr(VI) at pH 2.0, MO at pH 3.0, and their mixture at pH 3.0, respectively.

4 Conclusions

In conclusion, we have synthesized a new member of the guanidinium-based ICOF family through a simple Schiff-base condensation reaction. The ICOF presented high binding ability and fast adsorption kinetics for MO and Cr(VI) in their respective single pollutant systems, and also showed excellent simultaneous adsorption ability and good reusability for MO and Cr(VI). Moreover, it presented excellent binding selectivity for anionic pollutants. This work indicates the great potential of ICOFs as excellent sorbent materials for simultaneous removal of heavy metal ions and organic dyes in environmental remediation.

Conflicts of interest

There are no conflicts to declare.

Acknowledgements

This work was supported by the Scientific Research Foundation of Hunan Provincial Education Department (No. 20B586), Natural Science Foundation of Hunan Province (No. 2021JJ40525), and Hunan 2011 Collaborative Innovation Center of Chemical Engineering & Technology with Environmental Benignity and Effective Resource Utilization.

Notes and references

1 K. Li, P. Li, J. Cai, S. Xiao, H. Yang and A. Li, *Chemosphere*, 2016, **154**, 310–318.
2 J. Wang, W. Zhang and J. Wei, *J. Mater. Chem. A*, 2019, **7**, 2055–2065.
3 N. Velinov, J. Mitrović, M. Kostić, M. Radović, M. Petrović, D. Bojić and A. Bojić, *Wood Sci. Technol.*, 2019, **53**, 619–647.
4 J. Guo, X. Chen, Y. Shi, Y. Lan and C. Qin, *PLoS One*, 2015, **10**, e0134298.
5 S. Hassanpour, M. Taghizadeh and Y. Yamini, *J. Polym. Environ.*, 2017, **26**, 101–115.
6 Y. Yang, G. Wang, Q. Deng, D. H. Ng and H. Zhao, *ACS Appl. Mater. Interfaces*, 2014, **6**, 3008–3015.
7 Y. Lu, B. Jiang, L. Fang, F. Ling, J. Gao, F. Wu and X. Zhang, *Chemosphere*, 2016, **152**, 415–422.
8 P. Alulema-Pullupaxi, P. J. Espinoza-Montero, C. Sigcha-Pallo, R. Vargas, L. Fernandez, J. M. Peralta-Hernandez and J. L. Paz, *Chemosphere*, 2021, **281**, 130821.
9 J. Dasgupta, J. Sikder, S. Chakraborty, S. Curcio and E. Drioli, *J. Environ. Manage.*, 2015, **147**, 55–72.
10 R. Rakhunde, L. Deshpande and H. D. Juneja, *Crit. Rev. Environ. Sci. Technol.*, 2012, **42**, 776–810.
11 M. Herrero and D. C. Stuckey, *Chemosphere*, 2015, **140**, 119–128.
12 T. Jiang, W. Liu, Y. Mao, L. Zhang, J. Cheng, M. Gong, H. Zhao, L. Dai, S. Zhang and Q. Zhao, *Chem. Eng. J.*, 2015, **259**, 603–610.
13 N. S. Alsaiari, A. Amari, K. M. Katubi, F. M. Alzahrani, F. B. Rebah and M. A. Tahoon, *Processes*, 2021, **9**, 576–591.
14 S. P. Singh, K. Rathinam, R. Kasher and C. J. Arnusch, *RSC Adv.*, 2018, **8**, 27027–27036.
15 A. P. Côté, A. I. Benin, I. B. Annabelle, N. W. Ockwig, M. O'Keeffe, A. J. Matzger and O. M. Yaghi, *Science*, 2005, **310**, 1166–1170.
16 N. Huang, L. Zhai, H. Xu and D. Jiang, *J. Am. Chem. Soc.*, 2017, **139**, 2428–2434.
17 Y. Li, C. Wang, S. Ma, H. Zhang, J. Ou, Y. Wei and M. Ye, *ACS Appl. Mater. Interfaces*, 2019, **11**, 11706–11714.
18 Q. Lu, Y. Ma, H. Li, X. Guan, Y. Yusran, M. Xue, Q. Fang, Y. Yan, S. Qiu and V. Valtchev, *Angew. Chem., Int. Ed. Engl.*, 2018, **57**, 6042–6048.
19 X. H. Xiong, Z. W. Yu, L. L. Gong, Y. Tao, Z. Gao, L. Wang, W. H. Yin, L. X. Yang and F. Luo, *Adv. Sci.*, 2019, **6**, 1900547.
20 L. Zhang, Y. Li, Y. Wang, S. Ma, J. Ou, Y. Shen, M. Ye and H. Uyama, *J. Hazard. Mater.*, 2021, **407**, 124390.
21 A. R. Abdellah, H. N. Abdelhamid, A.-B. A. A. M. El-Adasy, A. A. Atalla and K. I. Aly, *J. Environ. Chem. Eng.*, 2020, **8**, 104054.
22 B. Dong, W. J. Wang, S. C. Xi, D. Y. Wang and R. Wang, *Chemistry*, 2021, **27**, 2692–2698.
23 Y. Li, C.-X. Yang, H.-L. Qian, X. Zhao and X.-P. Yan, *ACS Appl. Nano Mater.*, 2019, **2**, 7290–7298.
24 W. Tan, X. Wu, W. Liu, F. Ye and S. Zhao, *ACS Appl. Mater. Interfaces*, 2021, **13**, 4352–4363.
25 Y. Li, T. Hu, R. Chen, R. Xiang, Q. Wang, Y. Zeng and C. He, *Chem. Eng. J.*, 2020, **398**, 125566–125573.
26 S. Jansone-Popova, A. Moinel, J. A. Schott, S. M. Mahurin, I. Popovs, G. M. Veith and B. A. Moyer, *Environ. Sci. Technol.*, 2019, **53**, 878–883.
27 A. Lace, D. Ryan, M. Bowkett and J. Cleary, *Int. J. Environ. Res. Public Health*, 2019, **16**, 1803–1813.
28 H. J. Da, C. X. Yang and X. P. Yan, *Environ. Sci. Technol.*, 2019, **53**, 5212–5220.
29 S. Chen, Y. Huang, X. Han, Z. Wu, C. Lai, J. Wang, Q. Deng, Z. Zeng and S. Deng, *Chem. Eng. J.*, 2018, **352**, 306–315.
30 B. Saha and C. Orvig, *Coord. Chem. Rev.*, 2010, **254**, 2959–2972.
31 T. S. Khayyun and A. H. Mseer, *Appl. Water Sci.*, 2019, **8**, 170.
32 J. Lin and L. Wang, *Front. Environ. Sci. Eng. China*, 2009, **3**, 320–324.
33 C. A. Seipp, N. J. Williams, V. S. Bryantsev and B. A. Moyer, *Sep. Sci. Technol.*, 2017, **53**, 1864–1873.
34 X. Zhuang, J. Hao, X. Zheng, D. Fu, P. Mo, Y. Jin, P. Chen, H. Liu, G. Liu and W. Lv, *Sep. Purif. Technol.*, 2021, **274**, 118993–118999.